Modeling of Random Quasi-Phase-Matching in Birefringent Disordered Media

Jolanda S. Müller, Andrea Morandi, Rachel Grange⊙, and Romolo Savo⊙[*]

Optical Nanomaterial Group, Institute for Quantum Electronics, Department of Physics, ETH Zurich, Zurich, Switzerland

We provide a vectorial model to simulate second-harmonic generation (SHG) in birefringent, transparent media with an arbitrary configuration of nonlinear ($\chi^{(2)}$) crystalline domains. We apply this model on disordered assemblies of $LiNbO_3$ and $BaTiO_3$ to identify the influence of the birefringence on the random quasi-phase-matching process. We show that in monodispersed assemblies, the birefringence relaxes the domain size dependence of the SHG efficiency. In polydispersed assemblies with sufficiently large domains, we find that the birefringence introduces a SHG efficiency enhancement of up to 54% compared to isotropic reference crystals. This enhancement is domain size independent in non-phase-matchable materials, while it increases linearly with the domain size if the domains can be phase matched. These two different scaling behaviors are used in Kurtz and Perry's (KP) powder technique to identify the phase matchability of a material. We show on the example of $LiNbO_3$ and ammonium dihydrogen phosphate that the KP technique cannot be applied to domains smaller than the coherence length, because then the SHG scaling with the domain size becomes material specific.

Optical frequency conversion through phase matching in birefringent nonlinear ($\chi^{(2)}$) crystals has enabled a variety of applications in laser technology [1,2] and plays a key role in quantum source schemes [3]. The birefringence provides an orientation- and polarization-dependent refractive index, which is used to compensate for the phase lag accumulated by the mixing waves. This avoids the destructive interference of the generated waves, which starts to occur at lengths larger than the coherence length in any not phase-matched configuration. Random quasi-phase-matching (RQPM) is an alternative approach for removing destructive interference in optical frequency conversion [4,5]. It relies on the disordered distribution of the $\chi^{(2)}$ domains of certain media, such as polycrystalline materials [5–7], scattering powders [8–11] and bottom-up assembled photonic structures [12,13]. Under a pump excitation, the domains generate nonlinear waves with random phases and amplitudes. This leads to the cancellation of the interference terms and to the linear accumulation of the generated power with the number of domains. While RQPM is generally less efficient than phase matching, it provides numerous advantages, such as an ultrabroad acceptance bandwidth (tunability of the pump over hundreds of nanometers), the use of low-cost materials, and relaxed constraints on the polarization and the angle of incidence of the pump. These features make RQPM attractive for a variety of applications, such as optical parametric oscillators [14], ultrafast midinfrared lasers [15], and ultrafast autocorrelators [16]. The interest on RQPM has been largely focused on isotropic (i.e., nonbirefringent) crystals such as ZnSe, both experimentally and theoretically [5,17,18]—one reason for this is that RQPM enables taking advantage of the large nonlinearity of these isotropic crystals, even if they are non-phase-matchable.

First modeling of RQPM relied on the scalar approximation of both the optical field and the $\chi^{(2)}$ susceptibility of the domains [17,19]. Very recently, more comprehensive vectorial models have been developed to study the nonlinear speckle statistics [18] and the supercontinuum generation from isotropic disordered polycrystals [20]. SHG in birefringent disordered materials has only been modeled by averaging over the single-domain generation, without considering the effects of the propagation through the birefringent medium on the polarization states [21,22]. Up to now, no comprehensive model that explicitly accounts for the birefringence in RQPM has been presented.

Here, we introduce a vectorial model that considers the full three-dimensional rotation (i.e., full $\chi^{(2)}$ tensor) as well as the birefringence of each domain. The generation and propagation of the waves is calculated from domain to domain, considering the phases of the ordinary and extraordinary beam components separately. This is done within the approximation of no scattering at the domain-to-domain boundaries. We explore the effects of the birefringence on RQPM by calculating the second-harmonic generation (SHG) in disordered assemblies of lithium niobate ($LiNbO_3$) and barium

_____
[*]savor@phys.ethz.ch

titanate ($BaTiO_3$). We find that, in general, the birefringence is beneficial for RQPM. In monodispersed assemblies, the birefringence relaxes the domain size dependence of the SHG efficiency. In polydispersed assemblies, it introduces an efficiency enhancement of up to 54% compared to an isotropic reference material.

Thanks to the birefringence, our model can simulate domains in a phase-matchable regime, in which the SHG enhancement increases linearly with the domain size. This allows us to draw a comparison to the powder-characterization technique of Kurtz and Perry [8,22], which is widely applied to identify the phase matchability of a crystalline material. Contrary to the established behavior at large domain sizes, we find that the SHG scaling with the domain size cannot unequivocally identify the phase matchability of a crystal when the domain size is smaller than the coherence length.

I. MODEL

The presented model considers a disordered three-dimensional cuboid structure, consisting of quadratic ($\chi^{(2)} \neq 0$), birefringent, crystalline domains, as depicted in Fig. 1(a). Similarly to other models [17,18], the three-dimensional problem is reduced to a one-dimensional problem by breaking down the cuboid into multiple parallel one-dimensional sticks. The SHG of each individual stick is calculated separately. Figure 1(b) shows one disorder configuration of such a stick, in which the domains have random sizes and orientations. The domain size X_n is randomly chosen from a Gaussian distribution with an average domain size $\bar{X}$ and a polydispersity σ. The domain orientation is defined through the rotation between the laboratory frame ($\mathbf{x}'$,$\mathbf{y}'$,$\mathbf{z}'$) and the crystal frame of each domain ($\mathbf{x}$,$\mathbf{y}$,$\mathbf{z}$), with the Euler angles $(\varphi, \vartheta, \gamma)_n$, as shown in Fig. 1(c). For this, the laboratory frame axes are defined as the $\mathbf{z}'$ axis parallel to the propagation direction $\mathbf{k}$ and the two orthogonal directions $\mathbf{x}'$ and $\mathbf{y}'$, while the $\mathbf{z}$ axis is the optic axis of the crystal. For a uniform random distribution of crystal orientations, we randomly choose for each domain the rotation around $\mathbf{z}$ as $\varphi \in [0, 2\pi]$, the angle between $\mathbf{k}$ and $\mathbf{z}$ as $\vartheta = \arccos(u)$ with $u \in [-1, 1]$ [18], and the rotation around $\mathbf{k}$ as $\gamma \in [0, 2\pi]$. The refractive indices of the ordinary (o) and extraordinary (e) axes are given by n_o and $n_e(\vartheta) = [\sin(\vartheta)^2/(\bar{n}_e)^2 + \cos(\vartheta)^2/n_o^2]^{-1/2}$, with $\bar{n}_e$ the extraordinary refractive index at $\vartheta = \pi/2$ [1]. A visualization of the calculation process in one single domain is shown in Fig. 1(d). The incoming beam (pump) is defined as the plane wave (red)

$$\mathbf{E}(\omega) = (\hat{\mathbf{e}}_{x'} e^{i\phi_{x'}} \cos\beta + \hat{\mathbf{e}}_{y'} e^{i\phi_{y'}} \sin\beta) E_\omega e^{i(\mathbf{k}\cdot\mathbf{z}'-\omega t)}, \quad (1)$$

with amplitude E_ω, frequency ω, wave vector $\mathbf{k}$, the starting phases $\phi_{x'}$ and $\phi_{y'}$, and a polarisation angle β in the laboratory frame. The vectors $\hat{\mathbf{e}}_{x'}$ and $\hat{\mathbf{e}}_{y'}$ are the unit vectors

along the $\mathbf{x}'$ and $\mathbf{y}'$ axes. At the beginning of the domain, the electric fields in the laboratory frame $\mathbf{E}_{\text{lab}}$, are transformed into the reference frame of the respective crystal $\mathbf{E}_{\text{cry}} = R \cdot \mathbf{E}_{\text{lab}}$ [Fig. 1(c)], where $R = Z_1(\varphi)X_2(\vartheta)Z_3(\gamma)$ is the Euler-transformation matrix for a rotation around the original z axis $\mathbf{z}$ (rotation Z_1), around the new x axis $\hat{\mathbf{e}}_o$ (rotation X_2), and around the final z axis $\mathbf{k}$ (rotation Z_3) (see Sec. II A within the Supplemental Material [23]). In the crystal frame [Fig. 1(d)], the beams are decomposed into their components along the o and e axes and each polarization combination of the pump (oo, eo, oe, ee) generates a second-harmonic field $E_{\text{gen}}^u(2\omega, X_n)$ (blue) along $u \in \{o, e\}$, which is given at the end of the nth single domain according to (full derivation in Sec. II B,C within the Supplemental Material [23]):

$$E_{\text{gen}}^u(2\omega, X_n) = \sum_{v,w} \frac{i(2\omega)^2}{2\epsilon_0 c^2 k_3^u} P^{u,vw} \left(\frac{e^{i\Delta k^{u,vw} X_n} - 1}{i\Delta k^{u,vw}} \right) e^{ik_3^u X_n}. \quad (2)$$

With the phase mismatch $\Delta k^{u,vw} = k^v(\omega) + k^w(\omega) - k^u(2\omega)$, the wave vector k_3^u of the second harmonic along u, and $P^{u,vw} = \langle \hat{\mathbf{e}}_u, \mathbf{P}^{vw} \rangle$ the second-harmonic polarization along $v, w \in \{o, e\}$ projected onto the o and e axis ($\hat{\mathbf{e}}_u$ unit vector along $u \in \{o, e\}$), where $P_i^{vw} = 2\epsilon_0 \sum_{jk} d_{ijk} E_j^v E_k^w$. The second-order nonlinear tensor d_{ijk} is used in its contracted matrix form to calculate P_i^{vw} (see Sec. II B within the Supplemental Material [23]). The pump $\mathbf{E}(\omega, 0)$, as well as the total second harmonic from all previous crystals $\mathbf{E}_{\text{pre}}(2\omega, 0)$ are propagated through the domain. For both beams, the components along the o and e axis are propagated separately: $E^u(\omega, X_n) = E^u(\omega, 0)e^{ik^u(\omega)X_n}$. At the end of the domain, the propagated second-harmonic complex field from the previous domains is summed with the second-harmonic complex field generated in the current domain $E_{\text{tot}}^u(2\omega, X_n) = E_{\text{pre}}^u(2\omega, X_n) + E_{\text{gen}}^u(2\omega, X_n)$ [at the end of the domain in Fig. 1(d)]. The amplitude, polarization, and phase of the fields is explicitly considered in every step, such that the model can account for interference effects. The fields of the propagated pump $E^u(\omega, X_n)$ and the total second-harmonic field $E_{\text{tot}}^u(2\omega, X_n)$ are transformed back into the laboratory frame, forming the output of the nth domain. To simulate the propagation of the light through the stick, we implement a folding algorithm, which iteratively processes the sequence of domains. In each step, it takes the data of the current element (domain n) of the sequence and the result of the previous step (domain $n-1$) as input. The information is processed to generate the output of the nth domain, which then forms the input of the $(n+1)$th domain. The SHG intensities of each stick $I_{\text{stick}} = c\epsilon_0(|E_{\text{tot}}^{x'}|^2 + |E_{\text{tot}}^{y'}|^2)/2$ are averaged to yield the intensity of the cuboid.
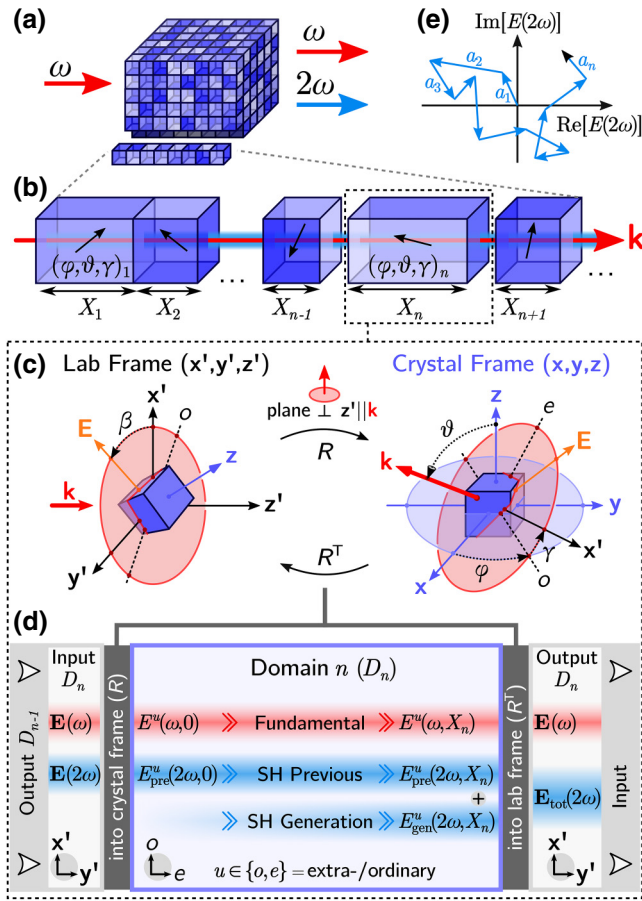
FIG. 1. (a) Sketch of a three-dimensional disordered assembly of second-order nonlinear domains, consisting of multiple parallel one-dimensional sticks. (b) Each stick contains domains of varying size X_n and orientation $(\varphi, \vartheta, \gamma)_n$, represented by the variation in color. (c) Depiction of the angles between the crystal frame $(\mathbf{x}, \mathbf{y}, \mathbf{z})$ and the laboratory frame $(\mathbf{x'}, \mathbf{y'}, \mathbf{z'})$ with the transformation matrix R. β is the polarization angle of the input beam in case of a linearly polarized beam ($\phi_{x'} = \phi_{y'}$). The ordinary and extraordinary axes are indicated with o and e. (d) Schematics of the process to propagate, generate and interfere the beams. The input electric fields (left) are transformed into the crystal frame and propagated to the end of the domain. They are then summed with the generated SHG from the current domain, and transformed back into the laboratory frame. (e) Phasor (a_n) representation of the interference between the second-harmonic waves generated by the domains within the stick. Each stick corresponds to a single random walk in the SHG complex plane, in which the step length is the amplitude of the second-harmonic field.

All simulations are performed using literature values of the $\chi^{(2)}$-tensor components and the o and e refractive indices, for LiNbO$_3$ [24,25], BaTiO$_3$ [26,27], and ammonium dihydrogen phosphate (ADP) [28,29]. Material properties are also provided in Sec. I A within the Supplemental Material [23].

In line with previous literature [17,18,20], the model uses the undepleted pump approximation [1], because the conversion efficiencies are always $\ll 1$ at the simulated pump intensity of 5.1×10^4 W/cm^2. We do not consider the absorption within the domains, as it is negligible at the studied wavelengths, both in BaTiO$_3$ and LiNbO$_3$ [30,31]. We also assume no reflection at the interfaces, since for domains with a regular shape (no sharp edges), it is estimated to be below 0.2% for both the pump as well as the SHG. Indeed, for the examined materials, the maximum refractive index mismatch is about 0.08 for the pump and 0.1 for the SHG. The small index mismatch and the size polydispersity of the domains makes it reasonable to assume that geometric resonances of the domains do not play a role in such systems. Lastly, we neglect spatial walk-off angles, which are typically small within a single domain [22]. In light of these assumptions, our model predicts the maximum possible SHG in the forward direction.

As an initial test of the algorithm, we compute the SHG in single crystals, phase-matched crystals and quasi-phase-matched systems [32] (see Sec. III A,B within the Supplemental Material [23]). In addition, we compute the SHG in structures characterized by mono- and polydispersed domain sizes without randomization of the domain orientation. These systems behave identically to a single crystal, periodically showing a totally constructive and destructive SHG along the length of the system. As expected, there is no dependence on the size distribution of the domains (see Sec. III A,B within the Supplemental Material [23]).

When introducing disorder in domain orientation and domain size, the SHG intensity of the single stick depends strongly on the specific disorder configuration. In this case, the SHG interference along the stick corresponds to the trajectory of a single random walk in the complex plane, as depicted in Fig. 1(e). As such, the SHG intensity of a single stick cannot be correlated with the number of domains N. Only upon averaging the intensities of multiple sticks (i.e., along the transverse dimensions of the cuboid), the total SHG intensity grows linearly with N, providing evidence of RQPM [17] (see Sec. II D within the Supplemental Material [23]). To identify and quantitatively study the effects stemming from the birefringence, we introduce the *isotropic analog* as a comparison alongside the birefringent material. The isotropic analog of a birefringent material is defined as the material that has the same $\chi^{(2)}$ tensor as the original material, but has isotropic linear refractive indices $\bar{n}_e = n_o$. Hence, the coherence length of the isotropic analog L_c^{iso} is not angle dependent. This stands in contrast to the coherence length in a birefringent material $L_c^{\mathrm{bir}}(\varphi, \vartheta, \gamma)_n$, which depends on the angle, as well as the combination of beam polarizations. Thus, a random distribution of the domain orientations does not affect the coherence length of isotropic domains, while it randomizes the coherence length of birefringent domains.

II. RESULTS

A. Monodispersed assemblies

One noteworthy result of this study, which is not exclusively related to birefringence, is that even monodispersed structures (without size randomisation) sustain RQPM, as long as the domains are randomly oriented. This is shown in Figs. 2(a) and 2(b) for LiNbO$_3$. The SHG efficiency per domain is measured by the slope of the linear growth, which depends on the domain size X. Its variation is represented by the shaded area and can be seen in the insets of Figs. 2(a) and 2(b), which report the SHG intensity as a function of the domain size. The isotropic analog, Fig. 2(a), shows a maximal efficiency when X is an odd multiple of L_c^{iso} and a minimal (zero) efficiency when X is an even multiple of L_c^{iso}. The latter case corresponds to the totally destructive SHG interference within the single domains. This is consistent with the results of Vidal *et al.* [17] at low polydispersity.

The effect of the birefringence is shown in Fig. 2(b). The maximal as well as the minimal efficiency is increased
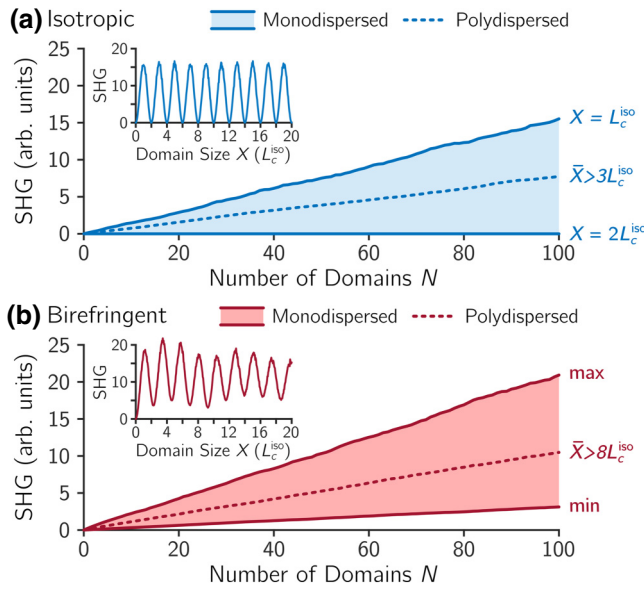

FIG. 2. Scaling of the SHG intensities with the number of domains N in birefringent LiNbO$_3$ and in its isotropic analog at a pump wavelength of 930 nm. SHG intensities are averaged over 1000 sticks, leading to a linear growth. Its slope represents the SHG efficiency for a certain domain size, and the shaded area shows the possible efficiencies in monodispersed assemblies. The insets explicitly show the SHG intensity in monodispersed assemblies only as a function of the domain size X for $N = 100$. In polydispersed assemblies ($\sigma = 30\%$) with large domains ($\bar{X} > 3\,L_c^{iso}$ in the isotropic and $\bar{X} > 8\,L_c^{iso}$ in the birefringent material) the efficiency has a stable value corresponding to the dotted line. (a) The isotropic analog has zero-efficiency minima when $\bar{X}$ is an even multiple of L_c^{iso}, and efficiency maxima when $\bar{X}$ is an odd multiple of L_c^{iso}. (b) The birefringent assembly has its minimum at $\bar{X} = 9.25\,L_c^{iso}$ and its maximum at $\bar{X} = 3.47\,L_c^{iso}$.

compared to the isotropic analog. In particular, the lower bound of the cone has a nonzero slope and the SHG never vanishes. Indeed, each birefringent domain has an orientation-dependent coherence length $L_c^{bir}(\varphi, \vartheta, \gamma)_n$, prompting that there is no specific domain size at which total destructive interference occurs for all domains. BaTiO$_3$ shows the same effect, but with a narrower cone of possible efficiencies (see Sec. IV within the Supplemental Material [23]).

The considered case of monodispersed assemblies highlights that polydispersity is neither a sufficient nor a necessary condition to achieve RQPM. This stands in contrast to the random orientation of domains, which plays a key role in reaching the RQPM regime.

B. Polydispersed assemblies

In Fig. 3(a) the SHG intensity of LiNbO$_3$ assemblies (red) and of their isotropic analog (blue) is shown for an increasing average domain size $0 \le \bar{X} \le 20\,L_c^{iso}$, a polydispersity $\sigma = 30\%$, and a fixed number of domains $N = 100$. Both curves follow the expected trend for RQPM [17]. In the small domain regime ($\bar{X} > L_c^{iso}$) the SHG intensity grows with the domain size without an appreciable difference between the birefringent and the isotropic case. Maximal intensities are reached when $\bar{X} = L_c^{iso}$, for the isotropic analog and for slightly larger domains in birefringent LiNbO$_3$. After an initial peak, the SHG gets independent of the average domain size, at approximately $3\,L_c^{iso}$ for the isotropic analog and at approximately $8\,L_c^{iso}$ for the birefringent LiNbO$_3$. In this stabilized large-domain regime, the SHG intensity of the birefringent LiNbO$_3$ is significantly larger than the stable value of the isotropic analog. Specifically, we observe a peak enhancement of $54 \pm 2\%$ at $3\,L_c^{iso}$. The effect is weaker in BaTiO$_3$, where the birefringence leads to a SHG enhancement of $9.25 \pm 0.8\%$ (see Sec. IV within the Supplemental Material [23]). The enhancement can also be seen on the slope of the dotted lines in Figs. 2(a) and 2(b), which report the linear scaling of the SHG intensity for assemblies with polydispersed domains at large domain sizes.

The origin of this overall enhancement lies in the distribution of the SHG intensities generated by the individual domains $I_{gen} = c\epsilon_0(|E_{gen}^o|^2 + |E_{gen}^e|^2)/2$ within the cuboid, which are shown in Fig. 3(b) for both the birefringent (red) and the isotropic (blue) LiNbO$_3$. These two SHG intensity distributions are obtained by extracting I_{gen} of the individual domains from the complete simulation depicted in Fig. 1(d), thus considering the specific polarization state of the pump (phase retardation between the o and e components) that the propagation through the previous birefringent domains introduced. The birefringence significantly widens the range of possible SHG intensities in the individual domains, due to the increased coherence
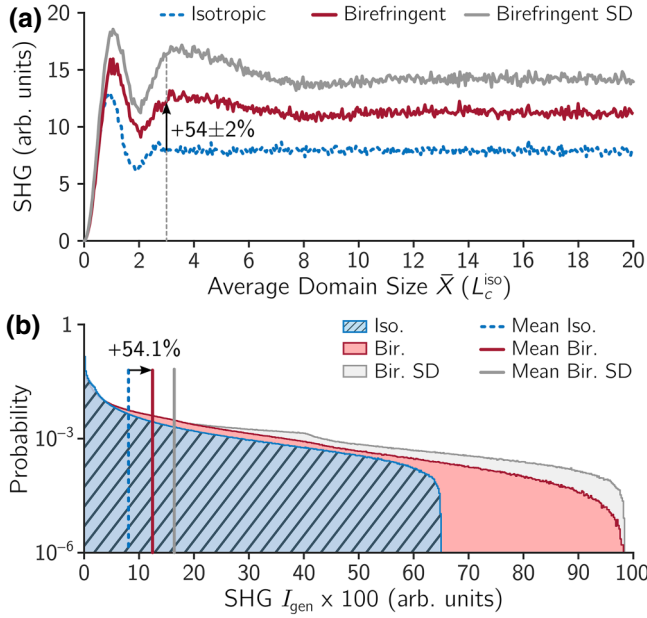
FIG. 3. (a) Scaling of the SHG intensity with the average domain size for disordered assemblies of isotropic LiNbO$_3$, birefringent LiNbO$_3$, and birefringent LiNbO$_3$ in the single domain (SD) approximation (single-domain average $\times N$). The assemblies have a domain size polydispersity $\sigma = 30\%$, a fixed number of domains per stick $N = 100$, an averaging over 1000 sticks, and are simulated at a pump wavelength of 930 nm. At this wavelength, phase matching in LiNbO$_3$ is not possible. (b) Probability distributions of the SHG intensities generated by the individual domains within the assembly ($\bar{X} = 3\,L_c^{\text{iso}}$ and $\sigma = 30\%$) for isotropic LiNbO$_3$, birefringent LiNbO$_3$, and birefringent LiNbO$_3$ in the SD approximation ($N = 1$, linearly polarized input beam). Probabilities are calculated as the relative frequency of appearance of a SHG intensity value over 10^7 domains. The SHG binning is 0.002. The SHG intensities are multiplied by 100 to be comparable with the intensities of the 100-domain assemblies in (a).

lengths $L_c^{\text{bir}}(\varphi, \vartheta, \gamma)_n > L_c^{\text{iso}}$ for certain domain orientations. Consequently, the average SHG intensity of the individual domains of birefringent LiNbO$_3$ is $54.1 \pm 0.3\%$ higher than the isotropic analog. Similarly for BaTiO$_3$, the enhancement is $9.24 \pm 0.1\%$, whose single-domain SHG intensity distribution is shown in Sec. IV within the Supplemental Material [23]. The enhancements of I_{gen} are consistent with the enhancement of the assembly calculated by considering the vectorial propagation of all components.

We highlight that the birefringence is only beneficial in domains larger than the isotropic coherence length $X_n > L_c^{\text{iso}}$. In smaller domains, the domain size X_n, rather than the coherence length, is the length scale limiting their SHG intensity (see Sec. V within the Supplemental Material [23]).

To underline the necessity of modeling the phase propagation between the domains, we calculate the SHG scaling

also in the single-domain (SD) approximation, i.e., by considering randomly oriented domains that are independently illuminated with a linearly polarized pump. Their average SHG is then multiplied by N to get the SHG efficiency of the assembly $I_{\text{tot}}^{\text{SD}} = N \times \langle I_{\text{gen}}^{\text{SD}} \rangle$. As shown in Fig. 3(a) (gray line), the SD approximation overestimates the SHG enhancement in the birefringent assembly of LiNbO$_3$ almost by a factor 2. This is because the SD approximation ignores the retardation introduced in the pump and hence calculates an inaccurate distribution of single-domain intensities, as shown in Fig. 3(b) (gray area). Isotropic materials, on the other hand, can be accurately simulated with the SD approximation, since they do not modify the polarization state of the pump.

C. Polydispersed assemblies under phase-matchable conditions

So far, we have performed our analysis in a non-phase-matchable regime. This means that the wavelengths have been chosen such that there is no crystal orientation for which phase matching is possible in the studied materials. Since our model considers birefringence, we can numerically investigate the phase-matchable regime in RQPM. For this, we consider LiNbO$_3$ at 1200 nm (see Sec. I B within the Supplemental Material [23]) and compare it to the non-phase-matchable regime by using the corresponding isotropic analog.

We investigate how the SHG scaling with the average domain size $\bar{X}$ is affected by the phase matchability of the domains, since this scaling behavior is considered experimentally to discriminate between phase-matchable and non-phase-matchable materials by using powder samples. This method was first introduced in the seminal work of Kurtz and Perry (KP) [8] and recently revised by Aramburu *et al.* [22].

The calculated SHG scalings with increasing average domain size $\bar{X}$ for LiNbO$_3$ and for its isotropic analog are shown in Fig. 4(a). To be comparable with KP, the length of the cuboid is kept fixed, which reduces the total number of domains when increasing the domain size. This rescales the SHG efficiency of Fig. 3 by $1/\bar{X}$, e.g., the constant SHG efficiency of the isotropic analog from Fig. 3 scales with $1/\bar{X}$ in Fig. 4. Another effect of the constraint on the total length of the cuboid, is the shift in the most efficient domain size from $\bar{X} \sim 1\,L_c^{\text{iso}}$ to $\bar{X} \sim 0.7\,L_c^{\text{iso}}$.

For comparison with the results reported by KP [8], we perform the same calculations on ADP, which are also shown in Fig. 4(a). Our model is able to reproduce the results obtained experimentally by KP in the large-domain regime ($\bar{X} > 5\,L_c^{\text{iso}}$). Namely, in the birefringent and phase-matchable case, the SHG intensity is independent of $\bar{X}$, while we observe a $1/\bar{X}$ dependence for its non-phase-matchable isotropic analog for both ADP and LiNbO$_3$. This implies that the enhancement of the SHG
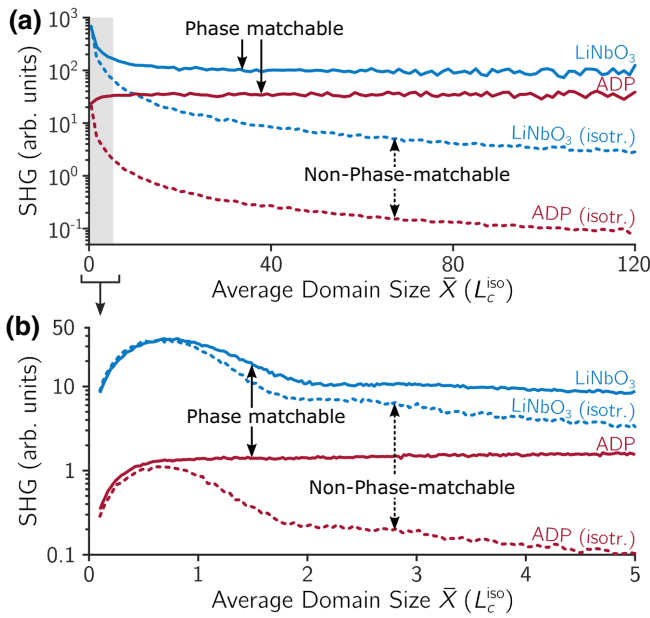
FIG. 4. Scaling of the SHG intensity with the average domain size $\bar{X}$ in disordered assemblies of LiNbO$_3$ and ADP and their isotropic analogs at a pump wavelength of $\lambda = 1200$ nm. At this wavelength, phase matching is possible in both materials. The total length of the sticks is kept constant and the domains have a polydispersity $\sigma = 30\%$. (a) The total length of the sticks is fixed at $1000\,L_c^{\text{iso}}$. When changing X, the number of domains per stick varies between 1000 domains (at $\bar{X} = 1\,L_c^{\text{iso}}$) to 10 domains (at $\bar{X} = 100\,L_c^{\text{iso}}$). The phase-matchable materials show a different scaling in comparison to their not phase-matchable isotropic analogs. Non-phase-matchable LiNbO$_3$ can also be simulated by using a shorter pump wavelength, which is shown in Sec. VI within the Supplemental Material [23]. (b) Higher-resolution simulation of the small-domain-size regime, performed at a reduced stick length of $50\,L_c^{\text{iso}}$ for computational efficiency. The shift in the y scale compared to (a) is due to the different stick length. In this small-domain regime the scaling of the SHG intensity is not determined solely by the phase matchability, but becomes material specific.

intensity, which is introduced by the birefringence, grows linearly with the average domain size as soon as some of the domains can be phase matched. This linear dependence is clearly visible when considering the SHG scaling without constraint on the cuboid length and with a fixed number of domains (Sec. VI within the Supplemental Material [23]).

Notably, the scaling behavior of the two materials is very different in the small-domain regime ($\bar{X} < 5\,L_c^{\text{iso}}$), as shown in Fig. 4(b). For ADP, one can see the monotonic increase in the phase-matchable case, while the non-phase-matchable case shows a SHG peak followed by a decreasing trend, in agreement with the results of KP [8]. Surprisingly, for LiNbO$_3$, there is no significant difference between the phase matchable and the non-phase-matchable case for $\bar{X} < 5\,L_c^{\text{iso}}$. Both show an initial peak followed

by a decreasing trend and they could not be distinguished by a scaling experiment. This result shows that for average domain sizes $\bar{X}$ smaller than $5\,L_c^{\text{iso}}$ the SHG scaling discovered by KP is not universal, but rather becomes material specific.

In LiNbO$_3$, the source of the deviation from the phase-matchable scaling of KP can be found in the largest tensor element d_{33}, which determines the $E_z \times E_z$ component of the SHG. This is a non-phase-matchable tensor element since the electric field of the SHG is orthogonal to the **z** axis for the ordinary beam component, and hence its contribution is zero in the phase-matchable configuration (*oo-e*). However, for randomly oriented domains smaller than L_c^{iso}, the contributions of the d_{33} tensor element dominate the total SHG. For such small domains the maximum SHG intensity is limited by the domain size rather than the coherence length. At larger domain sizes, the smaller—but phase-matchable—coefficient starts to contribute significantly to the total SHG and leads to the KP behavior. In ADP, all tensor components are the same, and therefore influence the phase-matchable and the non-phase-matchable SHG in equal parts. We conclude that only when the phase-matchable tensor components are much smaller than the non-phase-matchable ones, the disordered assembly behaves like the non-phase-matchable case of KP in the small-domain regime.

III. CONCLUSIONS

We develop a vectorial model that is capable of calculating the second-harmonic generation through RQPM in any transparent, birefringent, $\chi^{(2)}$-disordered medium. This gives the presented model a wide range of applicability: from single domains, to disordered assemblies, to assemblies with specific size and orientation correlations between the domains. We employ the presented model to explore the effects of the birefringence on the RQPM process, by considering fully disordered assemblies of LiNbO$_3$, BaTiO$_3$, and ADP in both non-phase-matchable and phase-matchable conditions. We pinpoint the role played by the birefringence through a comparison with isotropic analog materials having $\bar{n}_e = n_o$. While no influence of the birefringence is appreciable for smaller domains, the birefringence starts to play a notable role once the domains in the system are larger than the isotropic coherence length L_c^{iso} in three studied situations (monodispersed, polydispersed, and polydispersed with phase matching).

We identify the random orientation of the domains as the key feature to enter the RQPM regime, a property enabling RQPM even in monodispersed polycrystalline assemblies. With a proper choice of domain size, the monodispersed assembly can outperform the SHG efficiency of a polydispersed assembly in the large-domain regime. This property reveals the potential of the nonlinear

generation from layered structures (similar to periodically poled ones), which would require control of only the layer thickness, without restrictions in the crystal orientation. In this monodispersed case, the birefringence introduces a randomization of the coherence length that relaxes the domain size dependence of the SHG intensity. In polydispersed assemblies, the birefringence of the material leads to a domain-size-independent efficiency increase of up to 54% in comparison to the corresponding isotropic analog. This efficiency increase is ascribed to an increase in the average domain efficiency, stemming from larger coherence lengths for certain domain orientations.

We show that the explicit domain-to-domain propagation of the polarization components is necessary for the accurate prediction of this SHG efficiency enhancement and in general for the accurate description of the three-wave mixing process in disordered birefringent media.

We show that the Kurtz and Perry method to discriminate between phase-matchable and non-phase-matchable materials, cannot be applied when the domains are smaller than the coherence length, e.g., nanopowders. In this small-domain regime, the dependence of the SHG on the average domain size is given by the specific $\chi^{(2)}$ tensor of the domains and thus becomes material specific.

Our findings show how a larger set of materials, including birefringent crystals, can serve for RQPM applications and clarify the limitations of a widely applied method for the characterization of nonlinear optical materials. Due to the nonresonant nature of the SHG and the RQPM, we expect our results to be valid in a wide range of wavelengths (e.g., hundreds of nanometers for metal oxides), as long as the absorption is negligible.

The model could be extended to include absorption within the domains, scattering effects at the interfaces and other transport phenomena [33]. Moreover, it could be generalized to study other three-wave mixing processes such as sum- and difference-frequency generation and electro-optic effects.

ACKNOWLEDGMENTS

[1] R. W. Boyd, *Nonlinear Optics* (Elsevier, Academic Press London, 2008).

[2] E. Garmire, Nonlinear optics in daily life, Opt. Express **21,** 30532 (2013).

[3] P. G. Kwiat, K. Mattle, H. Weinfurter, A. Zeilinger, A. V. Sergienko, and Y. Shih, New High-Intensity Source of Polarization-Entangled Photon Pairs, Phys. Rev. Lett. **75,** 4337 (1995).

[4] S. E. Skipetrov, Nonlinear optics: Disorder is the new order, Nature **432,** 285 (2004).

[5] M. Baudrier-Raybaut, R. Haidar, P. Kupecek, P. Lemasson, and E. Rosencher, Random quasi-phase-matching in bulk polycrystalline isotropic nonlinear materials, Nature **432,** 374 (2004).

[6] R. Fischer, S. Saltiel, D. Neshev, W. Krolikowski, and Y. S. Kivshar, Broadband femtosecond frequency doubling in random media, Appl. Phys. Lett. **89,** 191105 (2006).

[7] J. Bravo-Abad, X. Vidal, J. L. D. Juárez, and J. Martorell, Optical second-harmonic scattering from a non-diffusive random distribution of nonlinear domains, Opt. Express **18,** 14202 (2010).

[8] S. K. Kurtz and T. T. Perry, A powder technique for the evaluation of nonlinear optical materials, J. Appl. Phys. **39,** 3798 (1968).

[9] J. F. de Boer, A. Lagendijk, R. Sprik, and S. Feng, Transmission and Reflection Correlations of Second Harmonic Waves in Nonlinear Random Media, Phys. Rev. Lett. **71,** 3947 (1993).

[10] S. Faez, P. Johnson, D. Mazurenko, and A. Lagendijk, Experimental observation of second-harmonic generation and diffusion inside random media, JOSA B **26,** 235 (2009).

[11] E. Makeev and S. Skipetrov, Second harmonic generation in suspensions of spherical particles, Opt. Commun. **224,** 139 (2003).

[12] P. Molina, M. Ramirez, and L. Bausá, Strontium barium niobate as a multifunctional two-dimensional nonlinear "photonic glass", Adv. Funct. Mater. **18,** 709 (2008).

[13] R. Savo, A. Morandi, J. S. Müller, F. Kaufmann, F. Timpu, M. Reig Escalé, M. Zanini, L. Isa, and R. Grange, Broadband mie driven random quasi-phase-matching, Nat. Photonics **14,** 740 (2020).

[14] Q. Ru, N. Lee, X. Chen, K. Zhong, G. Tsoy, M. Mirov, S. Vasilyev, S. B. Mirov, and K. L. Vodopyanov, Optical parametric oscillation in a random polycrystalline medium, Optica **4,** 617 (2017).

[15] S. Vasilyev, I. Moskalev, M. Mirov, S. Mirov, and V. Gapontsev, in *Ultrafast Bandgap Photonics*, edited by M. K. Rafailov and E. Mazur (International Society for Optics and Photonics (SPIE, 2016)), Vol. 9835, p. 94.

[16] R. Fischer, D. N. Neshev, S. M. Saltiel, A. A. Sukhorukov, W. Krolikowski, and Y. S. Kivshar, Monitoring ultrashort pulses by transverse frequency doubling of counterpropagating pulses in random media, Appl. Phys. Lett. **91,** 031104 (2007).

[17] X. Vidal and J. Martorell, Generation of Light in Media with a Random Distribution of Nonlinear Domains, Phys. Rev. Lett. **97,** 013902 (2006).

[18] T. Kawamori, Q. Ru, and K. L. Vodopyanov, Comprehensive Model for Randomly Phase-Matched Frequency Conversion in Zinc-Blende Polycrystals and Experimental Results for ZnSe, Phys. Rev. Appl. **11,** 054015 (2019).

[19] X. Chen and R. Gaume, Non-stoichiometric grain-growth in znse ceramics for $\chi^{(2)}$ interaction, Opt. Mater. Express **9,** 400 (2019).

[20] J. Gu, M. G. Hastings, and M. Kolesik, Simulation of harmonic and supercontinuum generation in polycrystalline media, JOSA B **37,** 1510 (2020).

[21] J. Trull, C. Cojocaru, R. Fischer, S. M. Saltiel, K. Staliunas, R. Herrero, R. Vilaseca, D. N. Neshev, W. Krolikowski, and Y. S. Kivshar, Second-harmonic parametric scattering in ferroelectric crystals with disordered nonlinear domain structures, Opt. Express **15,** 15868 (2007).

[22] I. Aramburu, J. Ortega, C. Folcia, and J. Etxebarria, Second harmonic generation by micropowders: A revision of the kurtz-perry method and its practical application, Appl. Phys. B **116,** 211 (2013).

[23] See Supplemental Material at http://link.aps.org/supplemental/10.1103/PhysRevApplied.15.064070 for material properties, algorithm details, and additional calculations and simulations.

[24] D. A. Roberts, Simplified characterization of uniaxial and biaxial nonlinear optical crystals: A plea for standardization of nomenclature and conventions, IEEE J. Quantum Electron. **28,** 2057 (1992).

[25] M. Hobden and J. Warner, The temperature dependence of the refractive indices of pure lithium niobate, Phys. Lett. **22,** 243 (1966).

[26] T. Zhao, H. Lu, F. Chen, G. Yang, and Z. Chen, Stress-induced enhancement of second-order nonlinear optical susceptibilities of barium titanate films, J. Appl. Phys. **87,** 7448 (2000).

[27] D. Zelmon, D. Small, and P. Schunemann, Refractive index measurements of barium titanate from.4 to 5.0 microns and implications for periodically poled frequency conversion devices, MRS Proc. **484,** 537 (2011).

[28] W. Martienssen and H. Warlimont, *Springer Handbook of Condensed Matter and Materials Data* (Springer, Berlin, Heidelberg, 2006).

[29] F. Zernike, Refractive indices of ammonium dihydrogen phosphate and potassium dihydrogen phosphate between 2000 å and 1.5 μ, JOSA **54,** 1215 (1964).

[30] E. Palik, *Handbook of Optical Constants of Solids: Volume 2* (Elsevier Science, Academic Press Cambridge, Massachusetts, 2012).

[31] E. Palik, *Handbook of Optical Constants of Solids, Five-Volume Set: Handbook of Thermo-Optic Coefficients of Optical Materials with Applications* (Elsevier Science, Academic Press Cambridge, Massachusetts, 1997).

[32] M. M. Fejer, G. Magel, D. H. Jundt, and R. L. Byer, Quasi-phase-matched second harmonic generation: Tuning and tolerances, IEEE J. Quantum Electron. **28,** 2631 (1992).

[33] R. Samanta and S. Mujumdar, Intensity-dependent speckle contrast of second harmonic light in a nonlinear disordered medium, Appl. Opt. **59,** 11266 (2020).